Electronic Supplementary Material (ESI) for Inorganic Chemistry Frontiers.
This journal is © the Partner Organisations 2023

MOFs for long-term gas storage: exploiting kinetic trapping in ZIF-8 for on-demand and stimuli-controlled gas release

Karsten Heinz,[a] Sven M. J. Rogge,[b] Andreas Kalytta-Mewes,[a] Dirk Volkmer[a] and Hana Bunzen[a],*

[a] Chair of Solid State and Materials Chemistry, Institute of Physics, University of Augsburg, Universitaetsstrasse 1, 86159 Augsburg, Germany
[b] Center for Molecular Modeling (CMM), Ghent University, Technologiepark-Zwijnaarde 46, B-9052 Ghent, Belgium

Content

1. Characterization of ZIF-8

All three ZIF-8 samples [i.e., **ZIF-8(s)**, **ZIF-8(m)** and **ZIF-8(l)**] were characterized by XRPD (Fig. S1), TGA (Fig. S2), FTIR (Fig. S3) and microscopy (Fig. S5).

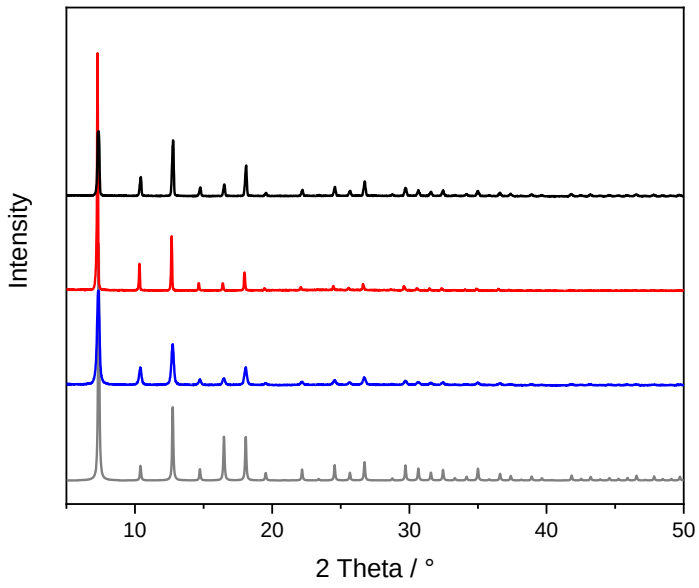

Figure S1. X-ray powder diffractograms of **ZIF-8(s)** (blue), **ZIF-8(m)** (red) and **ZIF-8(l)** (black), and their comparison to the calculated data from single crystal X-ray diffraction analysis (grey, CCDC: 602542).[1]

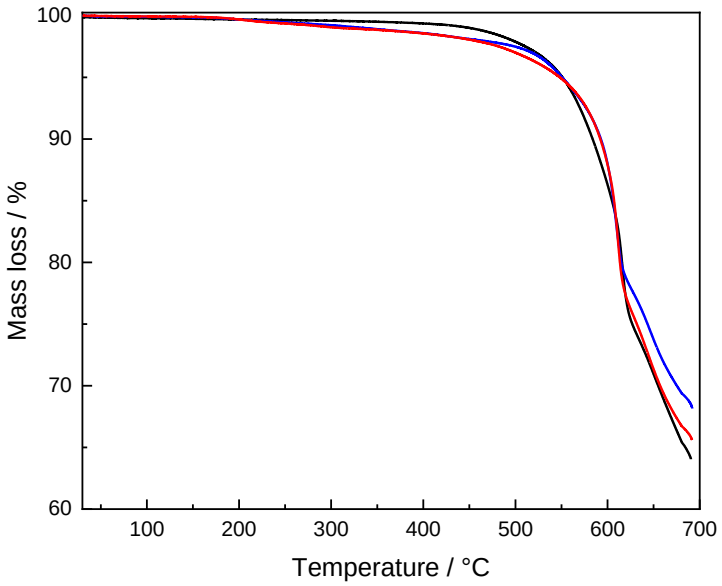

Figure S2. Thermogravimetric analysis of **ZIF-8(s)** (blue), **ZIF-8(m)** (red) and **ZIF-8(l)** (black) carried out under nitrogen atmosphere at a heating rate of 10 K min^{-1}.

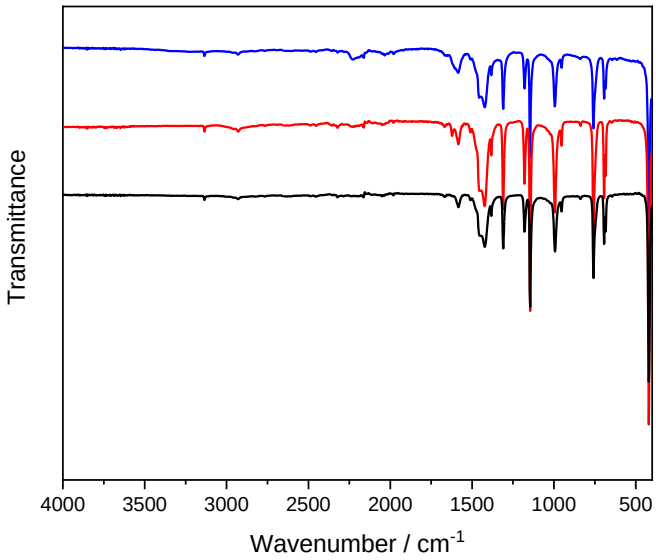

Figure S3. FTIR spectra of **ZIF-8(s)** (blue), **ZIF-8(m)** (red) and **ZIF-8(l)** (black).

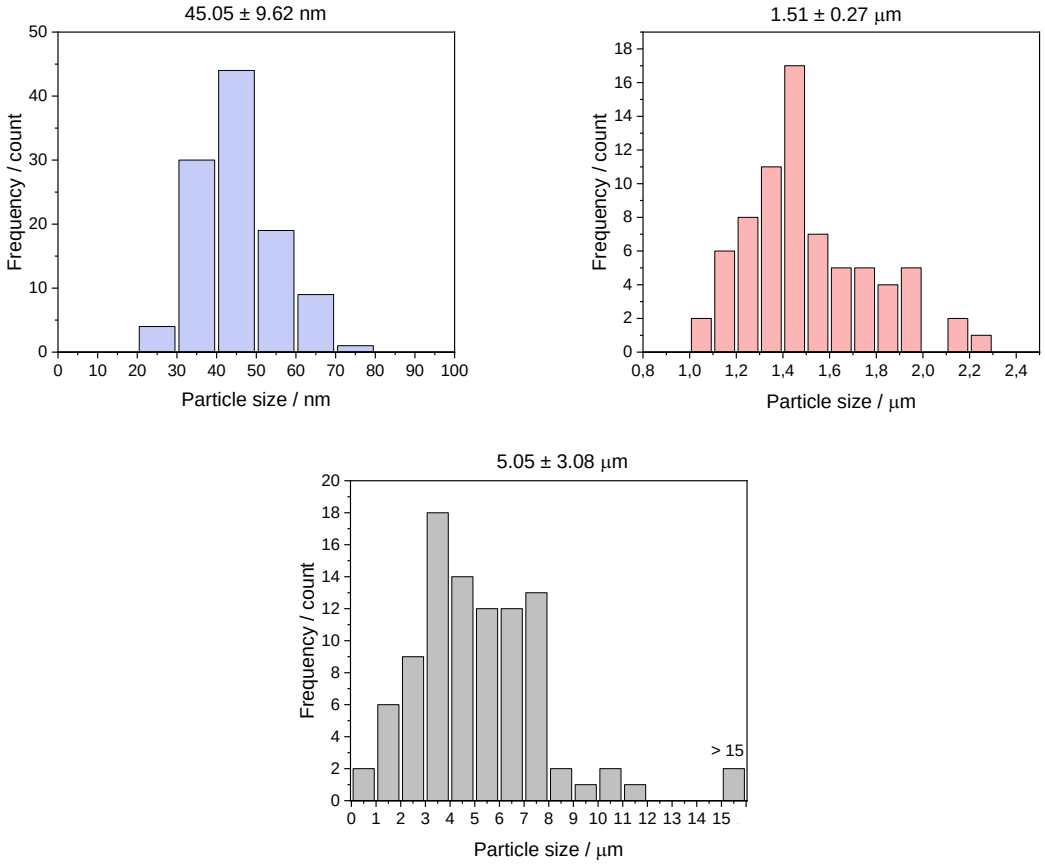

Figure S4. Particle size histograms of **ZIF-8(s)** (blue), **ZIF-8(m)** (red) and **ZIF-8(l)** (black) determined from SEM and STEM micrographs (examples shown in Figure S5) by analysing 100 particles.

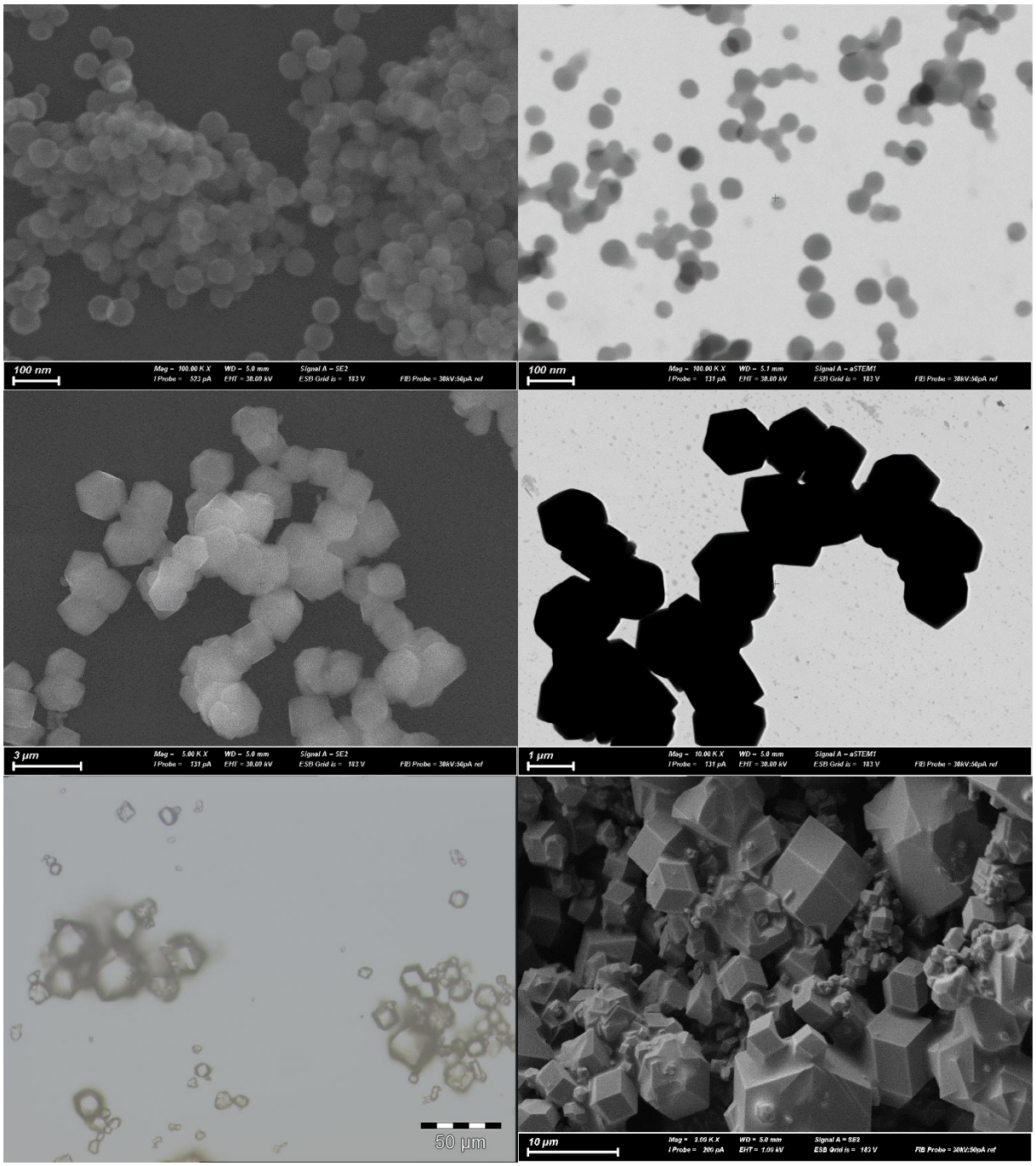

Figure S5. Electron and optical micrographs of crystals of ZIF-8; from top to bottom: **ZIF-8(s)**, **ZIF-8(m)** and **ZIF-8(l)**.

2. Loading of SF_6

Figure S6. Home-built apparatus for gas loading with a sample chamber shown in the inset.

Table S1. Overview of SF_6 loading into samples of **ZIF-8(s)** (1a-c), **ZIF-8(m)** (2a-e) and **ZIF-8(l)** (3a-f) at different loading temperatures. The optimised loading conditions are highlighted in a darker colour.

Sample name	SF_6 pressure (bar)	Temp. (° C)	Time (h)	SF_6 loaded (wt%)[a]	Number of SF_6 per pore	Density of SF_6 in the pore (g/cm^3)[b]	Mole of SF_6 in 1 g of ZIF-8 (mmol)	Corresponding volume of 'ideal gas' in 1 g of ZIF-8 (mL)[c]
1a	20	20	18	32.9	4.58	0.496	3.352	75.09
1a[d]	20	20	18	32.8	4.57	0.495	3.346	74.96
1b	20	50	18	31.2	4.24	0.471	3.106	69.57
1c	20	100	18	32.0	4.40	0.483	3.225	72.25
2a	20	20	18	6.2	0.61	0.093	0.450	10.08
2b	20	50	18	14.1	1.53	0.212	1.123	25.15
2c	20	100	18	23.3	2.83	0.351	2.074	46.46
2d	20	150	18	23.9	2.94	0.361	2.151	48.19
2d2[d]	20	150	18	23.3	2.83	0.351	2.076	46.50
2e	20	200	18	18.0	2.05	0.271	2.078	46.54
3a	20	20	18	1.1	0.10	0.016	0.073	1.64
3b	20	100	18	7.8	0.79	0.118	0.579	12.98
3c	20	150	18	12.7	1.36	0.192	0.998	22.36
3d	20	200	18	13.7	1.49	0.207	1.091	24.43
3e	20	250	18	13.5	1.45	0.203	1.065	23.86
3f[d]	20	200	42	18.5	2.12	0.279	1.551	34.74

[a] Determined by TGA (Fig. S7-S9).

[b] Calculated for the pore volume of 0.663 cm^3/g determined from XRD data.[1]

[c] According to the ideal gas law (one mole of an ideal gas at standard conditions has a volume of 22.4 L).

[d] Sample used for the gas release studies.

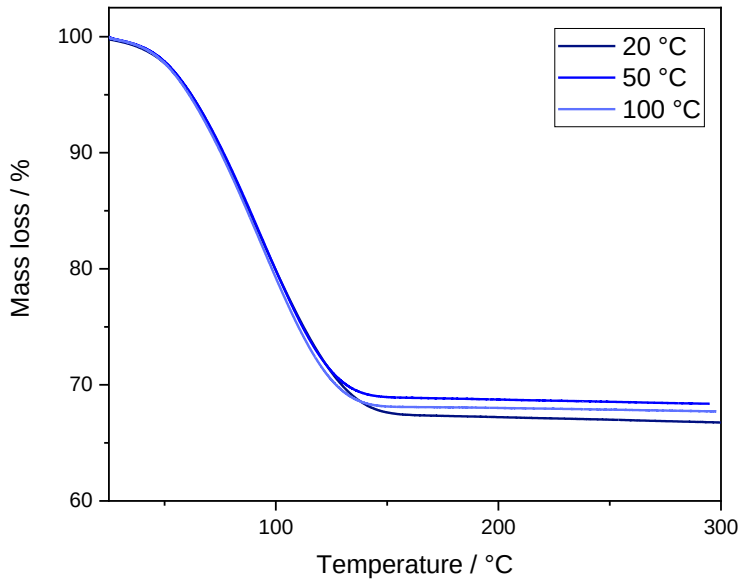

Figure S7. Thermogravimetric analysis of **ZIF-8(s)** loaded with SF_6 (Samples 1a-c, Table S1); measurements were carried out under a nitrogen atmosphere with a heating rate of 10 K min^{-1}.

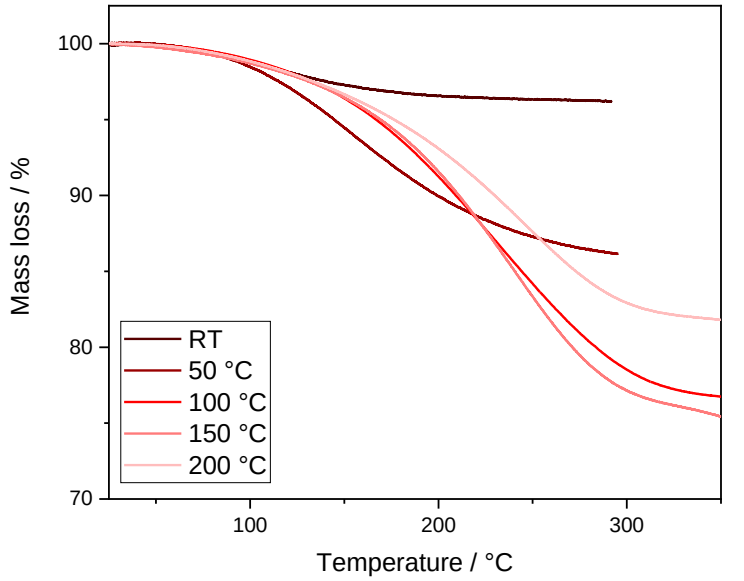

Figure S8. Thermogravimetric analysis of **ZIF-8(m)** loaded with SF_6 (Samples 2a-e, Table S1); measurements were carried out under a nitrogen atmosphere with a heating rate of 10 K min^{-1}.

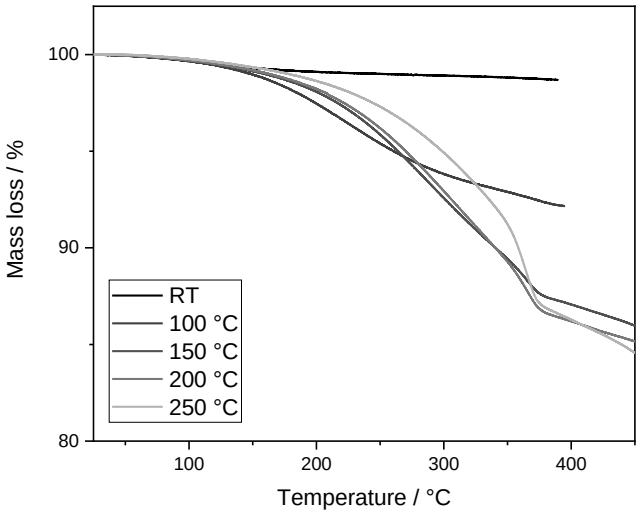

Figure S9. Thermogravimetric analysis of **ZIF-8(l)** loaded with SF_6 (Samples 3a-e, Table S1); measurements were carried out under a nitrogen atmosphere with a heating rate of 10 K min^{-1}.

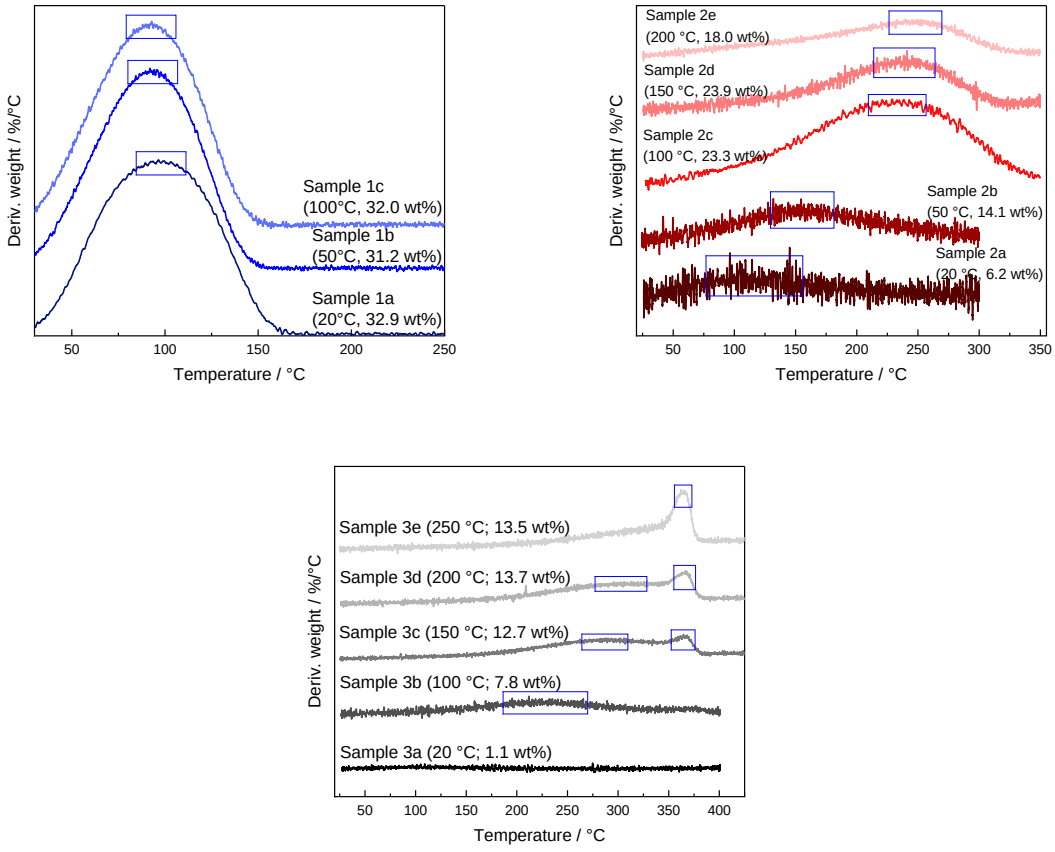

Figure S10. Derivative mass loss during thermogravimetric analyses of **ZIF-8(s)** (blue, Samples 1a-c, Fig. S7), **ZIF-8(m)** (red, Samples 2a-e, Fig. S8) and **ZIF-8(l)** (black, Samples 3a-e, Fig. S9). The area of a maximal gas release is marked in blue rectangles.

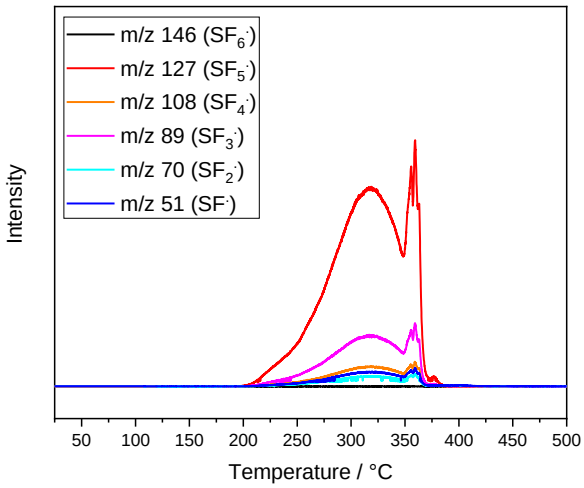

Figure S11. Temperature induced gas release from ZIF-8 loaded with SF_6 (Sample 3d) followed by mass spectrometry (EI); the measurement was carried out under an argon atmosphere at a heating rate of 5 K min^{-1}. Signals detected (m/z): 127 (SF_5^+), 108 (SF_4^+), 89 (SF_3^+), 70 (SF_2^+) and 51 (SF^+); Signals not detected (m/z): 146 (SF_6^+).

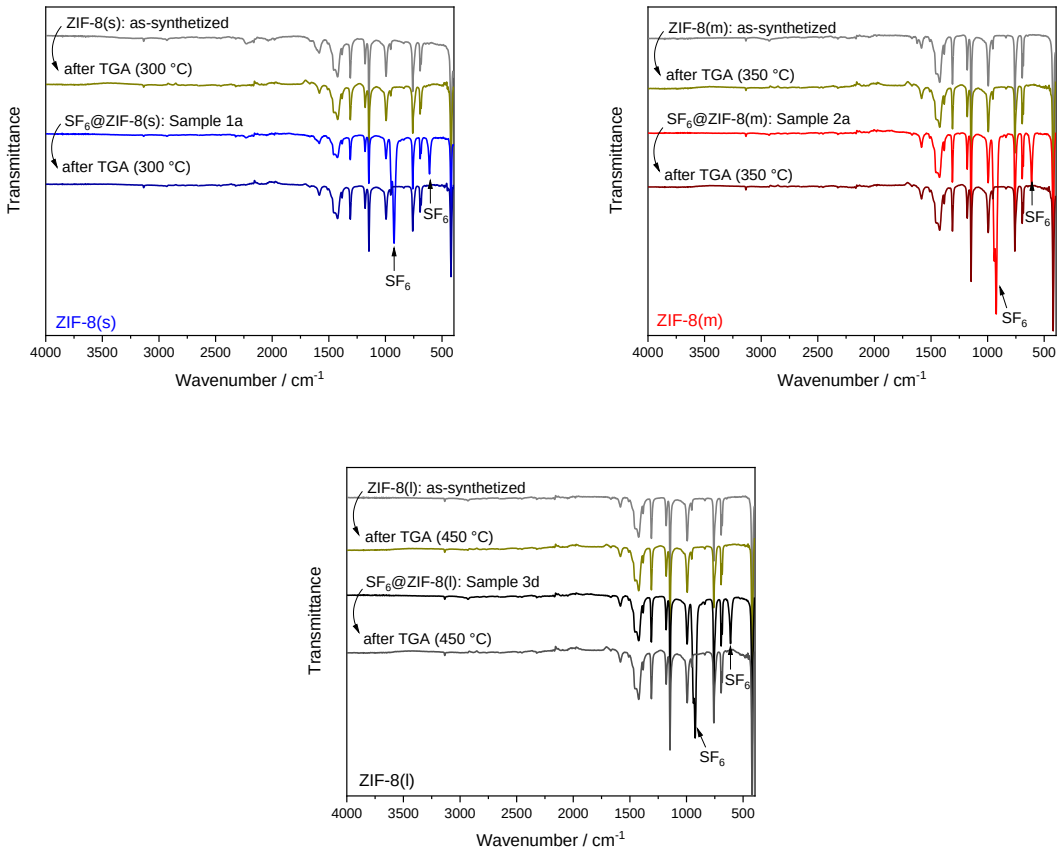

Figure S12. FTIR spectra of ZIF-8: (i) as-synthetized before and after TGA, and (ii) loaded with SF_6 before and after TGA [**ZIF-8(s)**: Sample 1a, heated up to 300 °C; **ZIF-8(m)**: Samples 2a, heated up to 350 °C; **ZIF-8(l)**: Sample 3d, heated up to 450 °C).

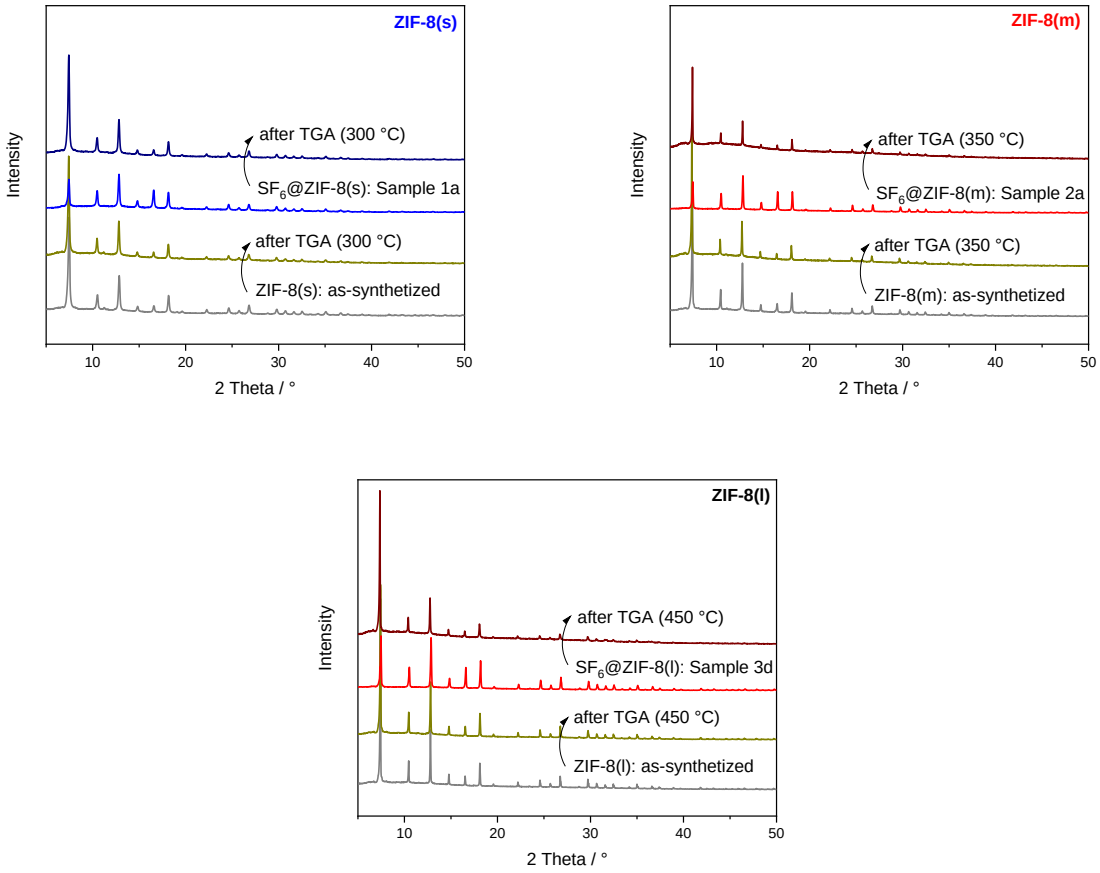

Figure S13. X-ray powder diffractograms of ZIF-8: (i) as-synthetized before and after TGA, and (ii) loaded with SF_6 before and after TGA [**ZIF-8(s)**: Sample 1a, heated up to 300 °C; **ZIF-8(m)**: Samples 2a, heated up to 350 °C; **ZIF-8(l)**: Sample 3d, heated up to 450 °C).

Table S2. Overview of vibration modes assigned to SF_6 as detected by FTIR spectroscopy (Fig. S12-S14).

Sample name	SF_6 loaded (wt%)[a]	v_3 vibration mode (cm^{-1})	v_4 vibration mode (cm^{-1})
1a	32.9	924.9 & 947.4	610.3
2d	23.9	923.3 & 941.1	611.1
3f	18.5	923.3 & 938.7	611.1
SF_6 (liquid)[2]	-	914.9	610.8
SF_6 (gas)[2]	-	948.0	614.5

[a] Determined by TGA (Table S1, Fig. S7-S9).

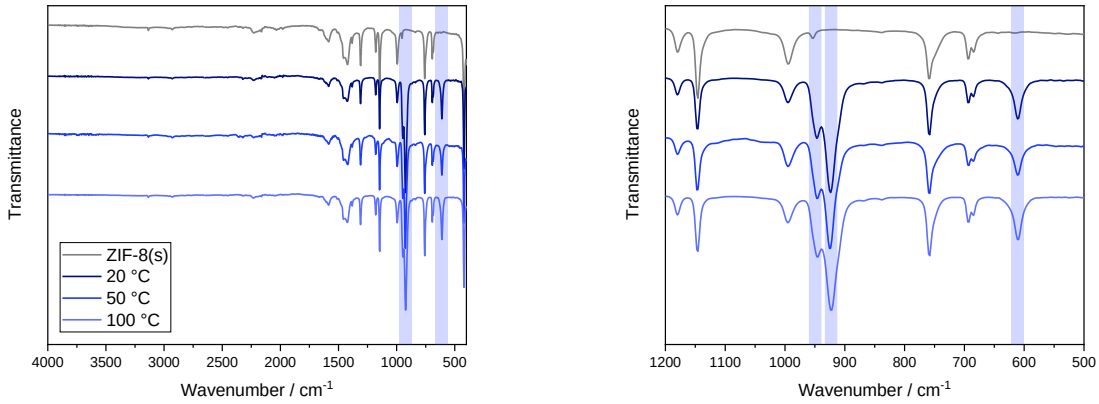

Figure S14. FTIR spectra of **ZIF-8(s)** loaded with SF_6 (Samples 1a-c, Table S1) and before the loading. Bands corresponding to SF_6 vibration modes are highlighted.

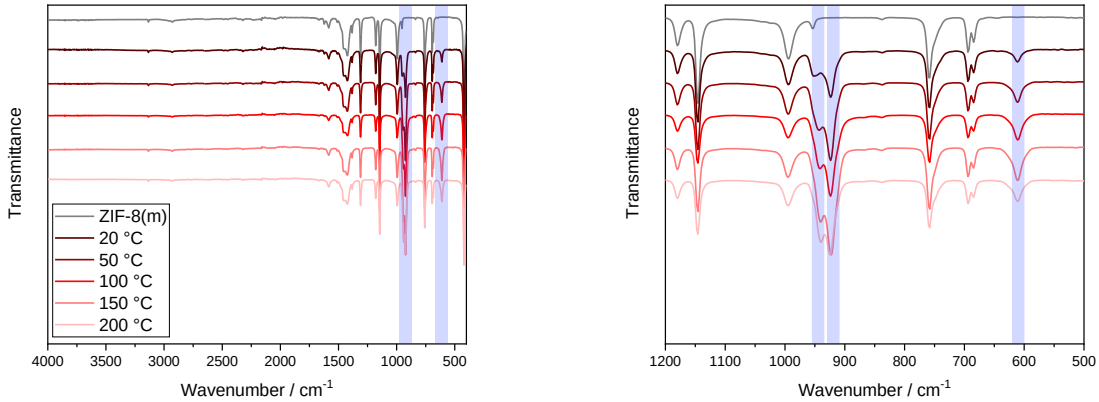

Figure S15. FTIR spectra of **ZIF-8(m)** loaded with SF_6 (Samples 2a-e, Table S1) and before the loading. Bands corresponding to SF_6 vibration modes are highlighted.

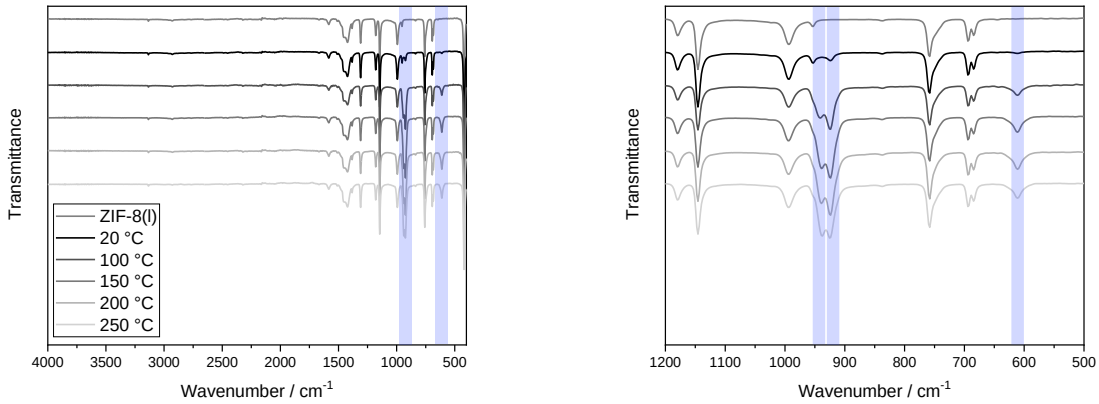

Figure S16. FTIR spectra of **ZIF-8(l)** loaded with SF_6 (Samples 3a-e, Table S1) and before the loading. Bands corresponding to SF_6 vibration modes are highlighted.

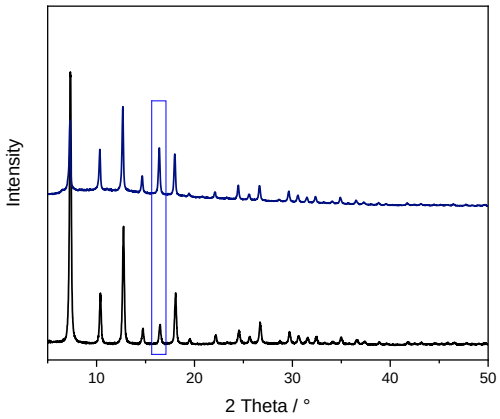

Figure S17. X-ray powder diffractograms of **ZIF-8(s)** loaded with SF_6 (Sample 1a) and before the loading. The diffraction peak at 16.4° with the most significant intensity change is marked in a blue rectangle.

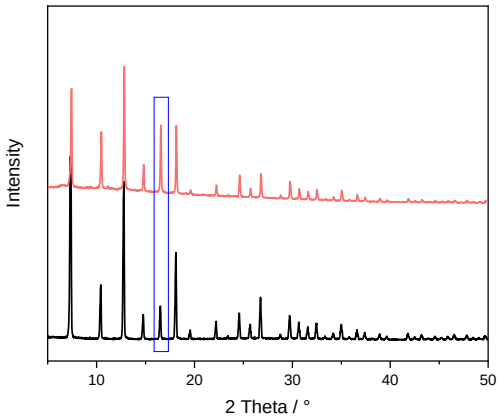

Figure S18. X-ray powder diffractograms of **ZIF-8(m)** loaded with SF_6 (Sample 2d) and before the loading. The diffraction peak at 16.4° with the most significant intensity change is marked in a blue rectangle.

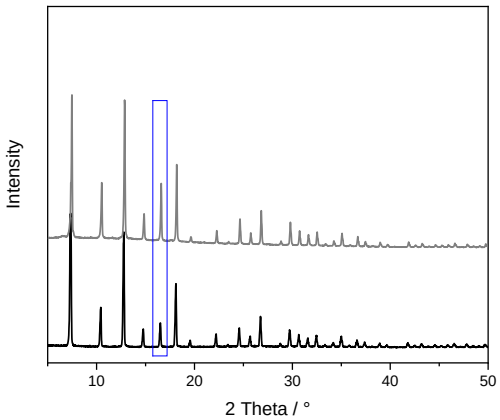

Figure S19. X-ray powder diffractograms of **ZIF-8(l)** loaded with SF_6 (Sample 3f) and before the loading. The diffraction peak at 16.4° with the most significant intensity change is marked in a blue rectangle.

3. Release of SF_6 at ambient conditions in air

Table S3. Overview of SF_6 release at ambient conditions in air from **ZIF-8(s)** (Sample 1a2), **ZIF-8(m)** (Sample 2d2) and **ZIF-8(l)** (Sample 3f) determined by TGA (Fig. S20-S22).

Sample 1a Time (days)	SF_6 loaded (wt%)[a]	Amount of SF_6 left (%)	Sample 2d Time (days)	SF_6 loaded (wt%)[a]	Amount of SF_6 left (%)	Sample 3f Time (days)	SF_6 loaded (wt%)[a]	Amount of SF_6 left (%)
0	32.83	100.00	0	23.28	100.00	0	18.47	100.00
1	25.31	77.09	1	21.95	94.27	1	18.38	99.49
2	17.23	52.49	3	20.67	88.77	3	17.06	92.39
4	9.79	29.82	5	19.77	84.91	7	16.99	91.96
6	5.71	17.40	9	18.97	81.49	14	17.18	93.02
9	4.00	12.18	14	18.22	78.27	21	16.89	91.45
11	3.05	9.29	28	18.18	78.10	28	16.57	89.73
14	1.48	4.51	42	17.00	73.00	42	16.82	91.08
21	0.83	2.53	60	16.40	70.46	60	16.68	90.32
28	0.77	2.35	100	16.03	68.85	100	15.91	86.14

[a] Determined by TGA (Fig. S18-S20).

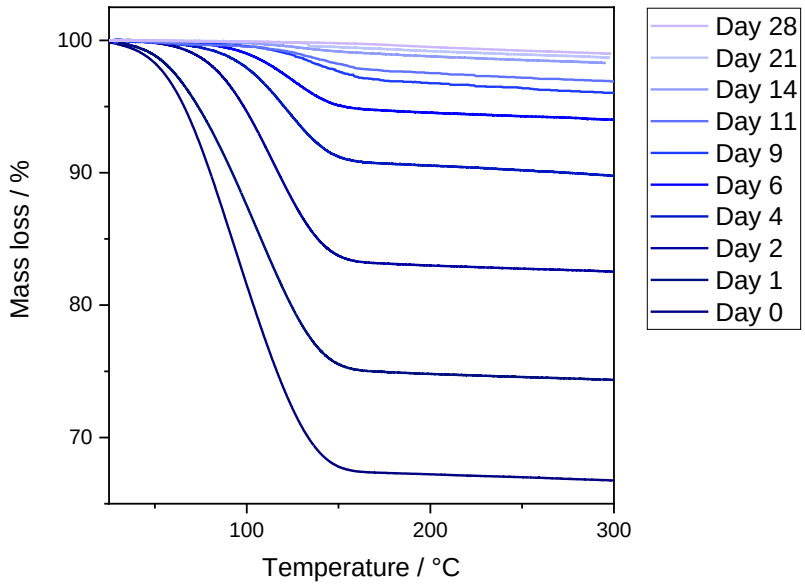

Figure S20. Thermogravimetric analysis of SF_6 release at ambient conditions in air from **ZIF-8(s)** (Sample 1a2); measurements were carried out under a nitrogen atmosphere with a heating rate of 10 K min^{-1}.

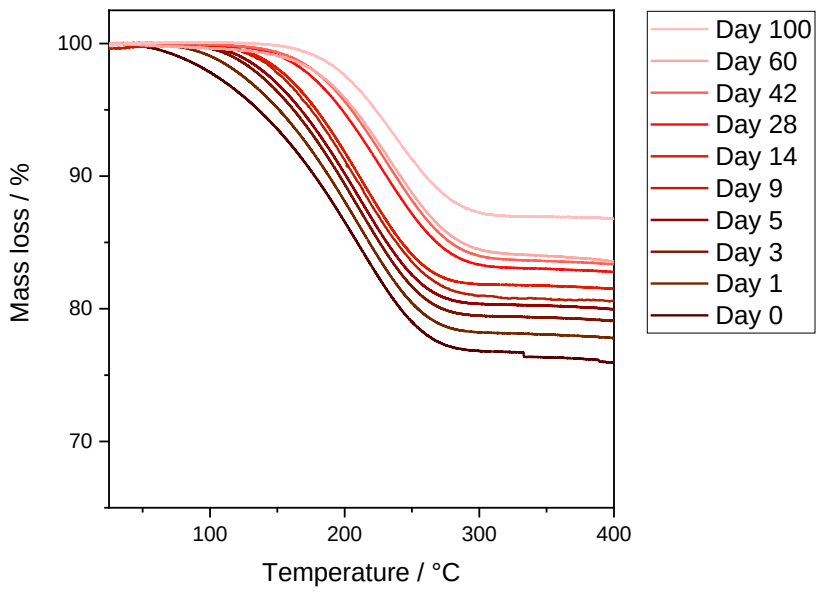

Figure S21. Thermogravimetric analysis of SF_6 release at ambient conditions in air from **ZIF-8(m)** (Sample 2d2); measurements were carried out under a nitrogen atmosphere with a heating rate of 10 K min^{-1}.

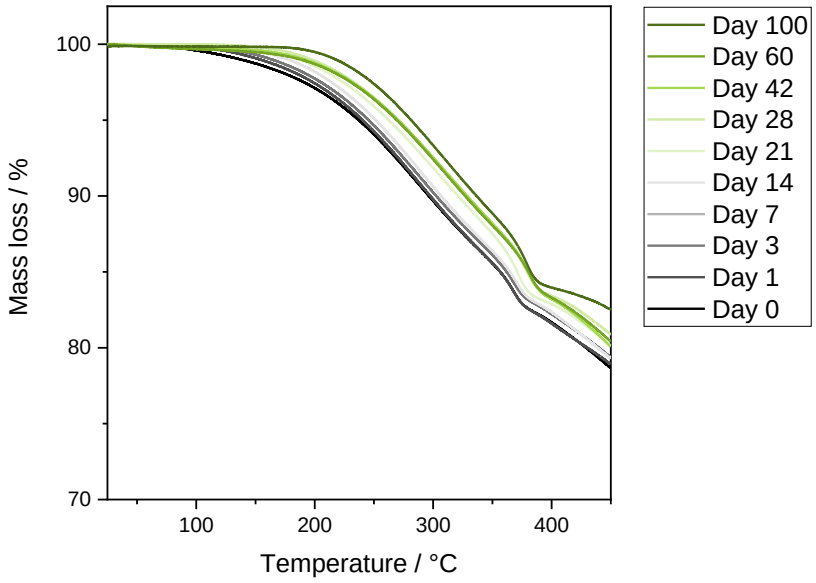

Figure S22. Thermogravimetric analysis of SF_6 release at ambient conditions in air from **ZIF-8(l)** (Sample 3f); measurements were carried out under a nitrogen atmosphere with a heating rate of 10 K min^{-1}.

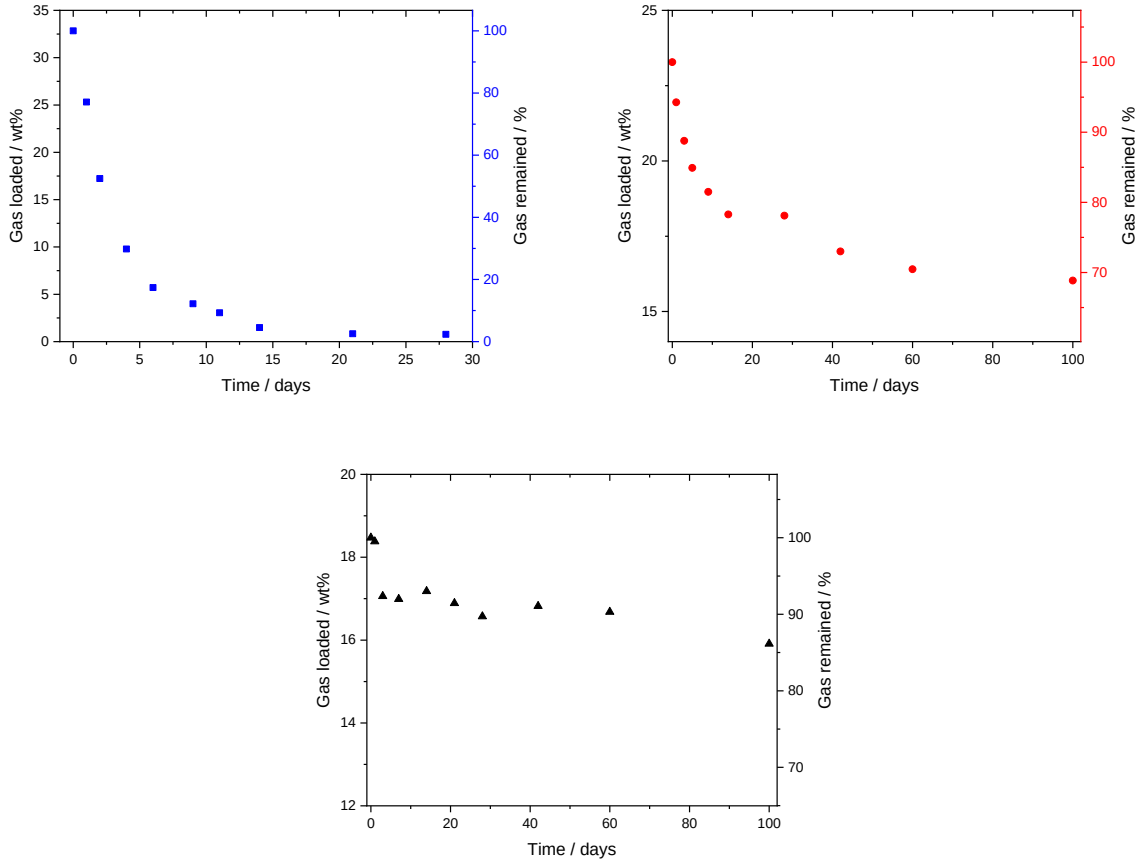

Figure S23. SF_6 release from **ZIF-8(s)** (blue, Sample 1a2), **ZIF-8(m)** (red, Sample 2d2) and **ZIF-8(l)** (black, Sample 3f) at ambient conditions in air determined by TGA (Fig. S20-S22, summarized in Table S2) shown in wt% of the total amount loaded (y-axis on the left) and in percentage of the gas remaining (calculated from the originally loaded amount; y-axis on the right).

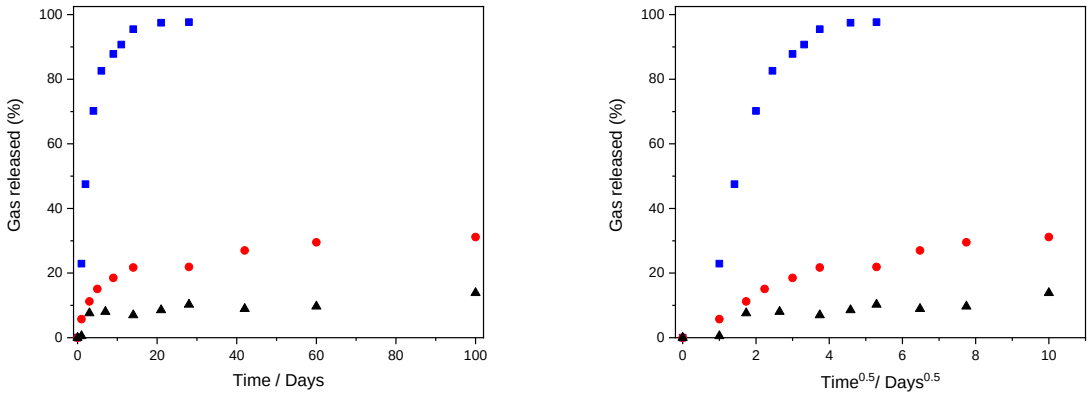

Figure S24. Release curves of SF_6 from **ZIF-8(s)** (blue), **ZIF-8(m)** (red) and **ZIF-8(l)** (black) expressed as percentage of the gas released in a linear time scale (left) and in square root of time scale (right).

For an isothermal system in which the release rate is controlled by intra-crystalline diffusion, the solution for the transient diffusion equation for a spherical particle is:

$$\frac{m_t}{m_\infty} = 1 - \frac{6}{\pi^2}\sum_{n=1}^{\infty}\frac{1}{n^2}\exp\left(\frac{-n^2\pi^2 Dt}{r^2}\right)$$

where *r* is the particle's radius and *D* the intra-crystalline (pore-network) diffusivity.[3] The diffusion time constants can be then calculated by linearly fitting $\ln(1-m_t/m_\infty)$ vs. *t* from the slope (Figure S25, Table S4).

$$\ln\left(1-\frac{m_t}{m_\infty}\right) = -\frac{\pi^2 D}{r^2}t + \ln\left(\frac{6}{\pi^2}\right)$$

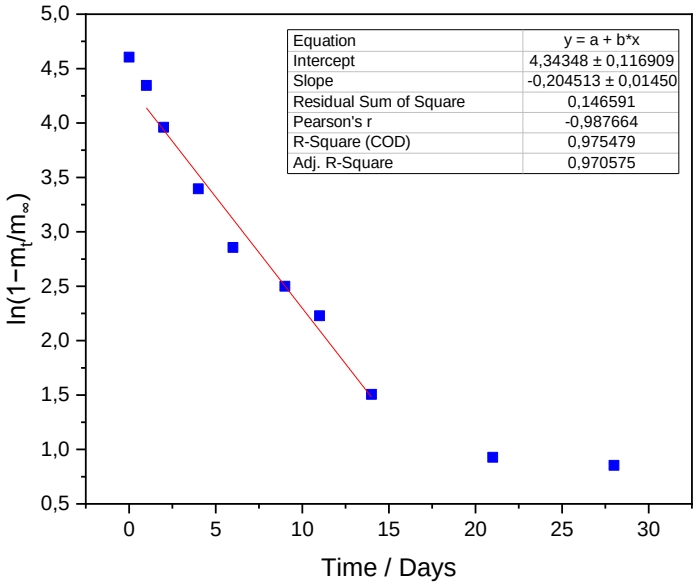

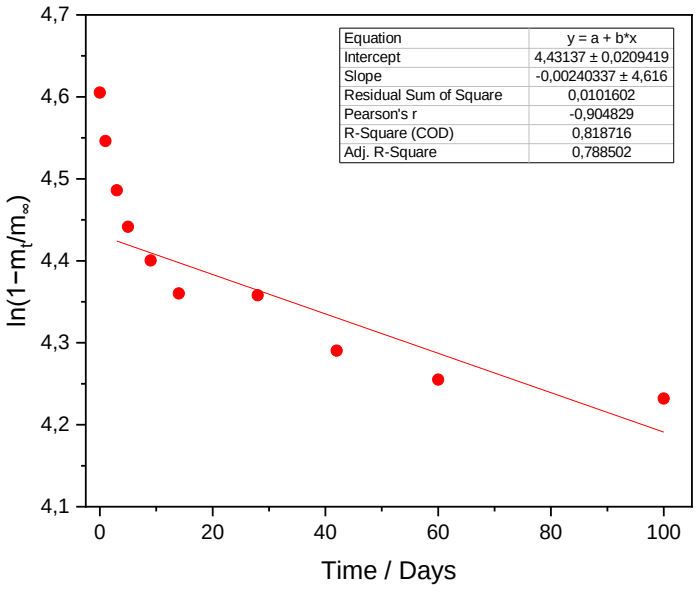

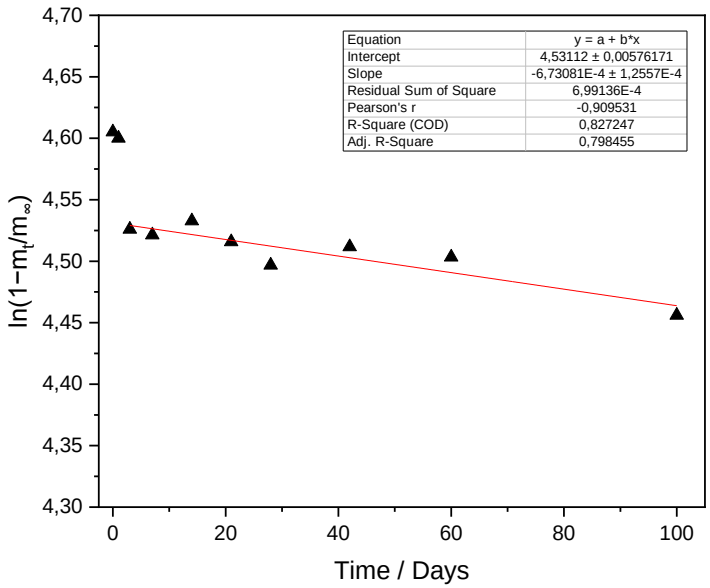

Figure S25. Release curves of SF_6 from **ZIF-8(s)** (blue), **ZIF-8(m)** (red) and **ZIF-8(l)** (black) analysed by the linearly fitting of $\ln(1-m_t/m_\infty)$ vs. t.

Table S4. Parameters determined by the linearly fitting $\ln(1-m_t/m_\infty)$ vs. t (Fig. S25), and results of the diffusion time constant calculation.

Sample	Slope	R-squared	Diffusivity ($\mu m^2\ day^{-1}$)	Diffusivity ($\mu m^2\ s^{-1}$)	Diffusivity ($m^2\ s^{-1}$)
ZIF-8(s)	-0.20451	0.9755	$1.05 \cdot 10^{-5}$	$1.21 \cdot 10^{-10}$	$1.21 \cdot 10^{-22}$
ZIF-8(m)	-0.002403	0.8187	$1.37 \cdot 10^{-4}$	$1.58 \cdot 10^{-9}$	$1.58 \cdot 10^{-21}$
ZIF-8(l)	-0.000673	0.8274	$4.26 \cdot 10^{-4}$	$4.93 \cdot 10^{-9}$	$4.93 \cdot 10^{-21}$

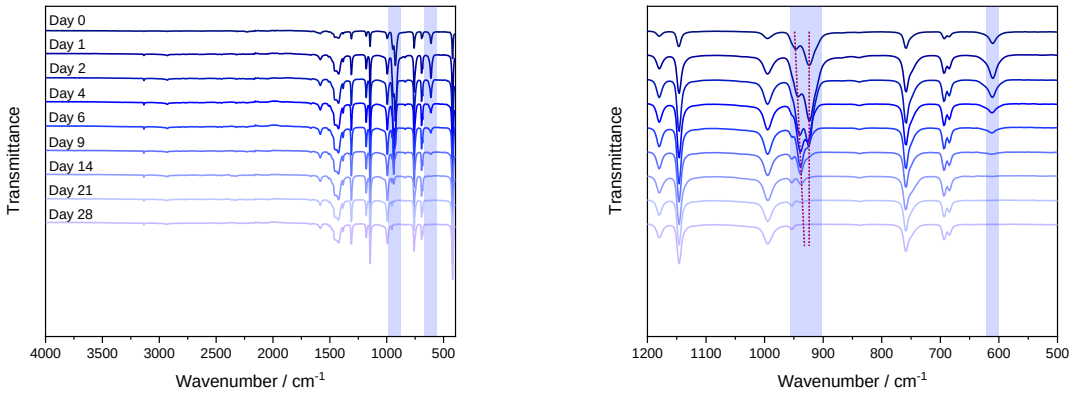

Figure S26. FTIR spectra of SF_6 release at ambient conditions in air from **ZIF-8(s)** (Sample 1a2). Bands corresponding to SF_6 vibration modes are highlighted.

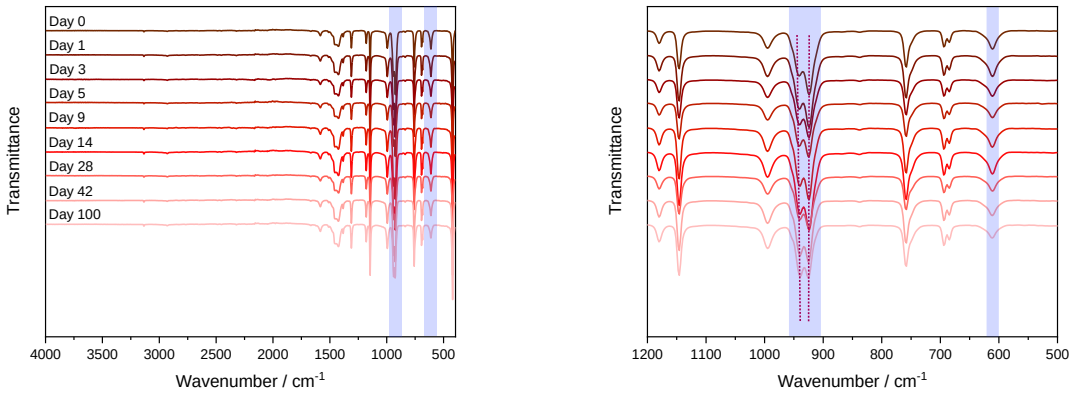

Figure S27. FTIR spectra of SF_6 release at ambient conditions in air from **ZIF-8(m)** (Sample 2d2). Bands corresponding to SF_6 vibration modes are highlighted.

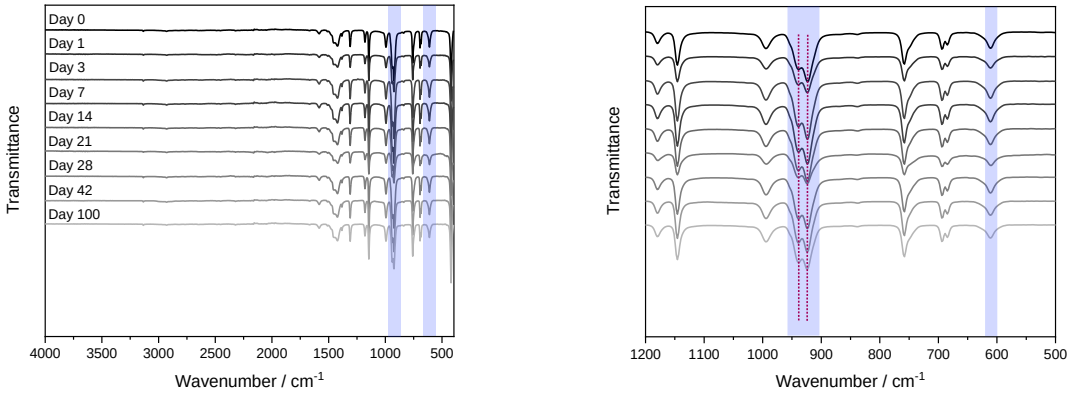

Figure S28. FTIR spectra of SF_6 release at ambient conditions in air from **ZIF-8(l)** (Sample 3f). Bands corresponding to SF_6 vibration modes are highlighted.

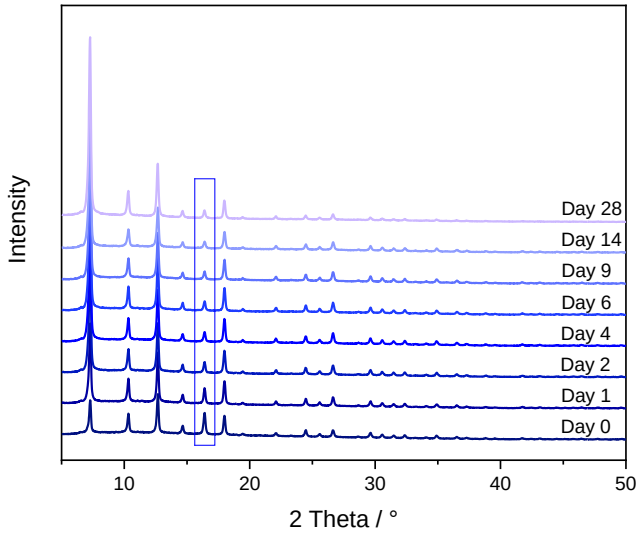

Figure S29. X-ray powder diffractograms of SF_6 release at ambient conditions in air from **ZIF-8(s)** (Sample 1a2). The diffraction peak at 16.4° with the most significant change in its intensity is marked in a blue rectangle.

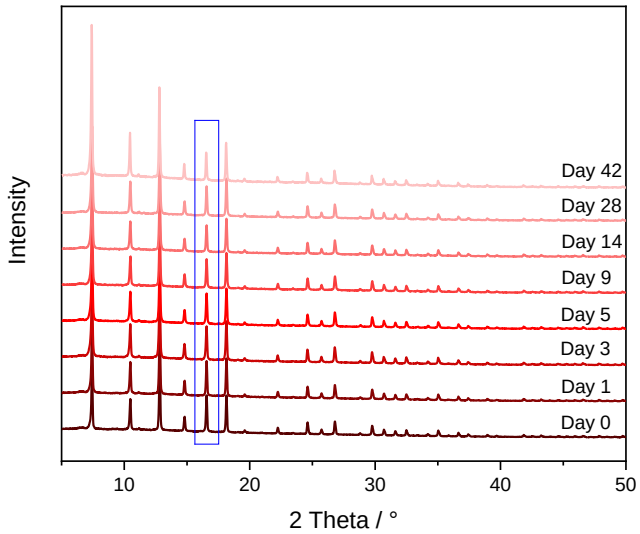

Figure S30. X-ray powder diffractograms of SF_6 release at ambient conditions in air from **ZIF-8(m)** (Sample 2d2). The diffraction peak at 16.4° with the most significant change in its intensity is marked in a blue rectangle.

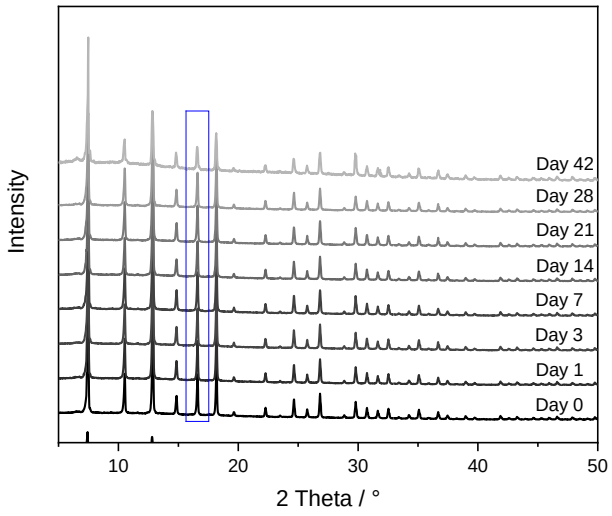

Figure S31. X-ray powder diffractograms of SF_6 release at ambient conditions in air from **ZIF-8(l)** (Sample 3f). The diffraction peak at 16.4° with the most significant change in its intensity is marked in a blue rectangle.

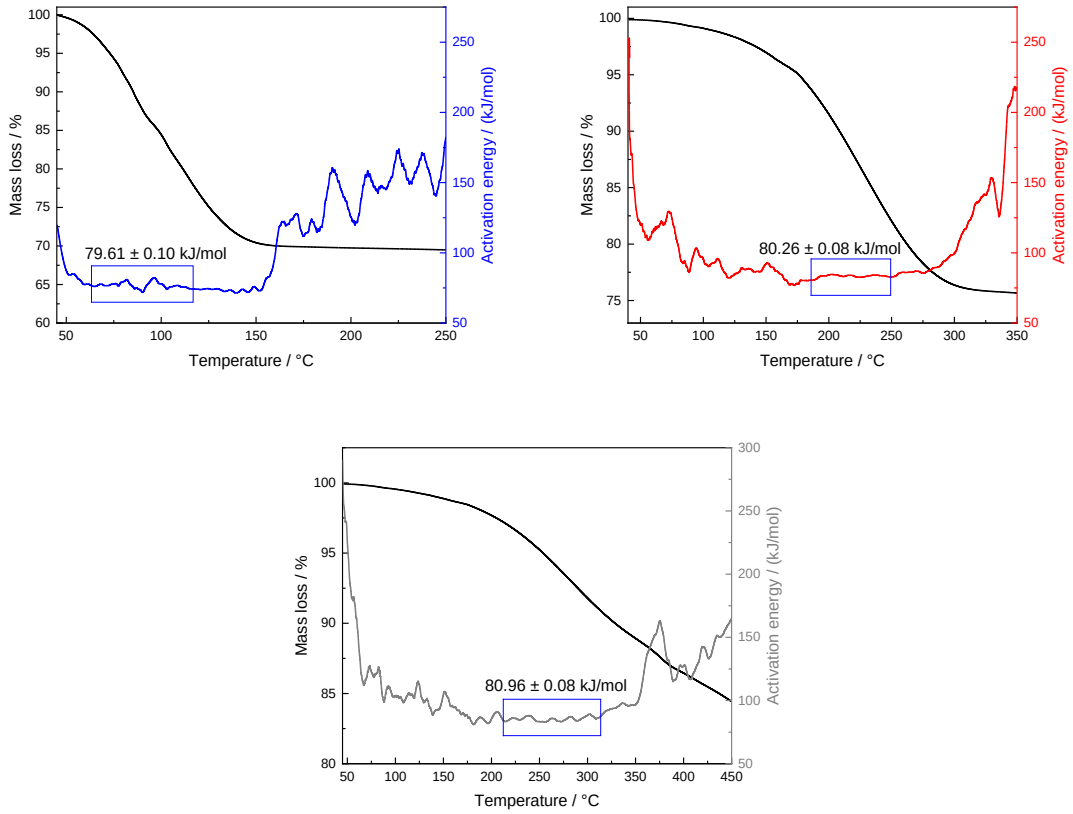

Figure S32. Temperature-modulated TG analyses of **ZIF-8(s)** (blue, Sample 1a2), **ZIF-8(m)** (red, Sample 2d2) and **ZIF-8(l)** (grey, Sample 3f) measured under a helium atmosphere at a heating rate of 1.5 K min^{-1}, amplitude of ± 5 °C and period of 200 s.

4. Acid-triggered gas release

Figure S33. Photographs of an acid-induced gas release from **ZIF-8(s)** loaded with SF_6 (Sample 1a2). A sample of **ZIF-8(s)** (ca. 5 mg) was exposed to a 2M aqueous solution of HCl (ca. 0.15 mL). To improve the visualization of the gas release, the sample was layered with diethyl ether (ca. 0.9 mL) before the acid was added; however, the layering is not necessary and does not affect the result of the experiment.
A video capturing the experiment as well as a control experiment without the loaded gas guest is available as Electronic Supplementary File.

5. Computational methods

The procedure to arrive at the free energy profiles reported in Fig. 4 of the main text consists of four main steps, as discussed in the main text. These steps are detailed below; representative input scripts for all steps described here are available at https://github.com/SvenRogge/supporting-info.

5.1 Deriving a system-specific DFT-based force field

Similar to our earlier work on water intrusion in ZIF-8,[4] we described the interactions in the flexible SF_6@ZIF-8 system using a system-specific force field derived from DFT data following the QuickFF procedure.[5,6] To this end, the existing and extensively validated ZIF-8 force field derived in Ref. 4 was adopted and supplemented with a new force field to describe the interactions in SF_6 as well as between SF_6 and the ZIF-8 framework.
The SF_6 molecule was DFT optimized using the B3LYP exchange-correlation functional[7,8] and the 6-311G(d,p) basis set, as implemented in the Gaussian 16 software suite.[9] The electrostatic interactions in the force field were modelled as Coulomb interactions between Gaussian charge distributions, for which the atomic charges were computed using the Minimal Basis Iterative Stockholder (MBIS) partitioning method[10], whereas the Gaussian radii were determined based on the approach of Chen and Martínez.[11] The DFT optimized SF_6 structure and Hessian were then used to determine the covalent interactions in the force field using QuickFF, excluding any cross terms given the small size of the molecule.[5,6] Finally, the van der Waals parameters of the MM3 force field by Allinger *et al.* were adopted to describe the dispersion interactions.[12] The so obtained force field for SF_6 was then combined with the existing one for ZIF-8 derived in Ref. 4.

5.2 Defining the collective variable

The collective variable (CV) adopted here is visualized in Figure S35 and requires two ingredients. First, the relative position of the centroid of the constrained SF_6 molecule (making the transition between the two

pores) with respect to the centre of the six-membered ring (6MR) aperture separating pore 1 and pore 2 is calculated. Second, the normal on the plane of the 6MR is defined in such a way that it points from pore 1 to pore 2. The used CV is then defined as the orthogonal projection of this first relative position on this normal. The same CV was also adopted in Ref. 4 (for ZIF-8) and Ref. 13 (for H-SAPO-34).

5.3 Selecting initial structures for the umbrella sampling simulations

Initially, two force-field based molecular dynamics (MD) simulations were performed in the $(N, P, \boldsymbol{\sigma}_a = \mathbf{0}, T)$ ensemble[14] at a temperature of 300 K and a pressure of 10 bar and using a 2x2x2 ZIF-8 supercell to avoid potential, spurious interactions between periodic images of the SF_6 molecules. In this setup, all ZIF-8 pores were empty, except for a single pore (defined as pore 1) that contained either four or six SF_6 molecules. These preliminary MD simulations were performed for 0.5 ns using the velocity Verlet integration scheme and a Verlet time step of 0.5 fs. They were performed using the Yaff software,[15] which was interfaced with LAMMPS to efficiently calculate the long-range interactions.[16] Temperature and pressure were controlled using a Nosé-Hoover chain thermostat with three beads and a time constant of 0.1 ps,[17-20] and using a Martyna-Tobias-Klein barostat with a time constant of 1 ps,[21,22] respectively. A smooth cut-off radius of 12 Å was adopted for the van der Waals interactions, which was compensated by tail corrections. The electrostatic interactions were efficiently calculated using an Ewald summation with a real-space cut-off of 12 Å, a splitting parameter α of 0.213 $Å^{-1}$ and a reciprocal space cut-off of 0.32 $Å^{-1}$.[23] The MD simulations with four and six SF_6 molecules showed very similar results. Especially, neither simulation exhibited a spontaneous transition of one of the SF_6 molecules from their initial pore to an adjacent pore, evidencing the high free energy barrier for the transition. Therefore, to select initial structures for the subsequent US simulations, the following procedure was used starting from the MD simulation with six SF_6 molecules. First, for each of the six SF_6 molecules and for each point in the MD trajectory, the CV value was calculated. Then, for each of the 45 equidistant target CV values between -11 Å and 11 Å with a step of 0.5 Å, we checked whether any of the observed CV values came within 0.25 Å of the target value. If this was the case, the snapshot with the smallest deviation for that target CV value was extracted as initial snapshot for the subsequent US simulation at that target CV value. If this was not the case, such as for all CV values exceeding -2 Å given the large free energy around this region, appropriate snapshots were created by selecting the SF_6 molecule with the CV value closest to the target value, and by moving this molecule as a rigid body along the 6MR normal used to define the CV until it attained the target CV value.

Using the above procedure, 45 initial structure were obtained for the US simulations in which five additional SF_6 molecules are present in pore 1 besides the one SF_6 molecule making the transition. To account for all other initial loadings, the required number of molecules were deleted from pore 1.

5.4 Performing the umbrella sampling simulations

The umbrella sampling simulations were performed in the $(N, V, \mathbf{h}_0, T)$ ensemble[14] at a temperature of 300 K, again using a 2x2x2 ZIF-8 supercell and starting from the initial structures defined above. All computational settings were the same as for the aforementioned MD simulations; the total simulation time for each simulation was 1 ns of which 0.1 ns was discarded for equilibration. For each of the six loadings (with in between zero and five additional SF_6 molecules in pore 1) and for each of the 45 target CV values, an umbrella sampling was performed using a harmonic bias potential centred on this target CV value and with a bias force constant of 25 kJ mol^{-1} $Å^{-2}$. As shown in Figure S34, this bias strength simultaneously ensures that the probability distributions of adjacent US simulations overlap and that these probabilities are centred around the target CV value, except for a small region around the 6MR window at CV = 0 Å. To improve the overlap in this region, additional US simulations were performed between -3 Å and 3 Å for all six loadings and with bias strengths of 50, 75, 100, 150, 200, and 300 kJ mol^{-1} $Å^{-2}$. At this highest bias strength, the overlap between adjacent probability distributions was observed to be

sufficient. All simulations for a given loading where then used as input for the weighted histogram analysis method (WHAM),[24,25] resulting in the free energy profiles discussed in Figures 4, S35, and S36.

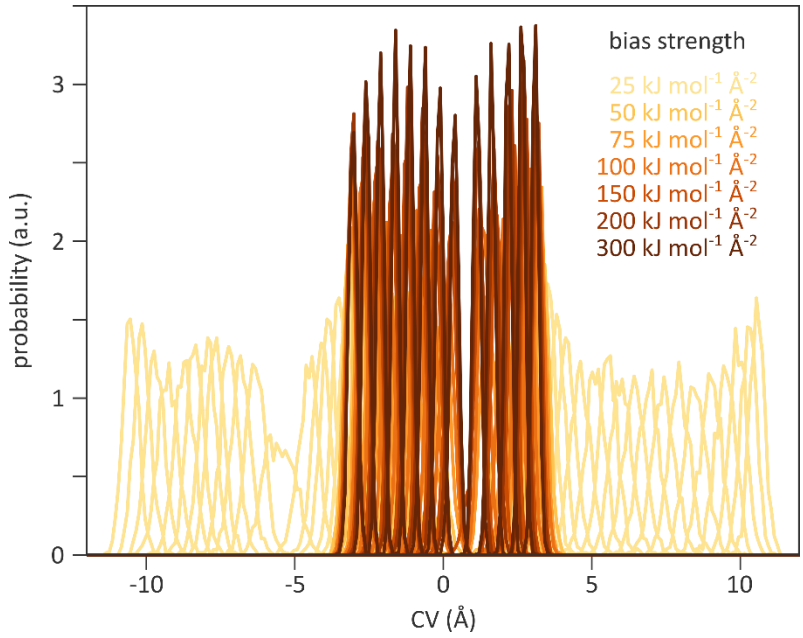

Figure S34. Probability of the sampled CV values for each of the 300 K US simulations in which three additional SF_6 molecules are present in pore 1. Besides the original US simulations with a bias strength of 25 kJ mol^{-1} $Å^{-2}$, additional US simulations were performed in the range [-3 Å, 3 Å] with bias strengths of 50, 75, 100, 150, 200, and 300 kJ mol^{-1} $Å^{-2}$ to ensure that the transition region is sampled adequately.

6. Computational free energy barriers for gas release

To computationally predict the free energy barrier for a SF_6 molecule to move from one ZIF-8 pore to an adjacent pore, a procedure similar to the one used in Ref. 4 was used. A series of US simulations were performed in which each simulation constrains the SF_6 molecule around a certain location. This location is defined by the CV shown in Figure S35, which determines whether the SF_6 molecule is in the first pore (CV < 0 Å) or in the second, adjacent pore (CV > 0 Å). The 6MR separating both pores is defined by CV = 0 Å and is expected to be responsible for the high activation barrier. This US protocol was necessary as SF_6 molecules were not observed to spontaneously move from one pore to another pore during a regular MD simulation at 300 K and 10 bar, a consequence of the large free energy barrier. By performing an US simulation, in which a free energy bias is added to the system at a given CV value, the constrained SF_6 molecule is forced to remain close to that given CV value. By repeating this procedure for all different CV values describing the SF_6 molecule moving from the first pore to the second pore, a full free energy profile can be constructed from which the free energy barrier can be extracted.

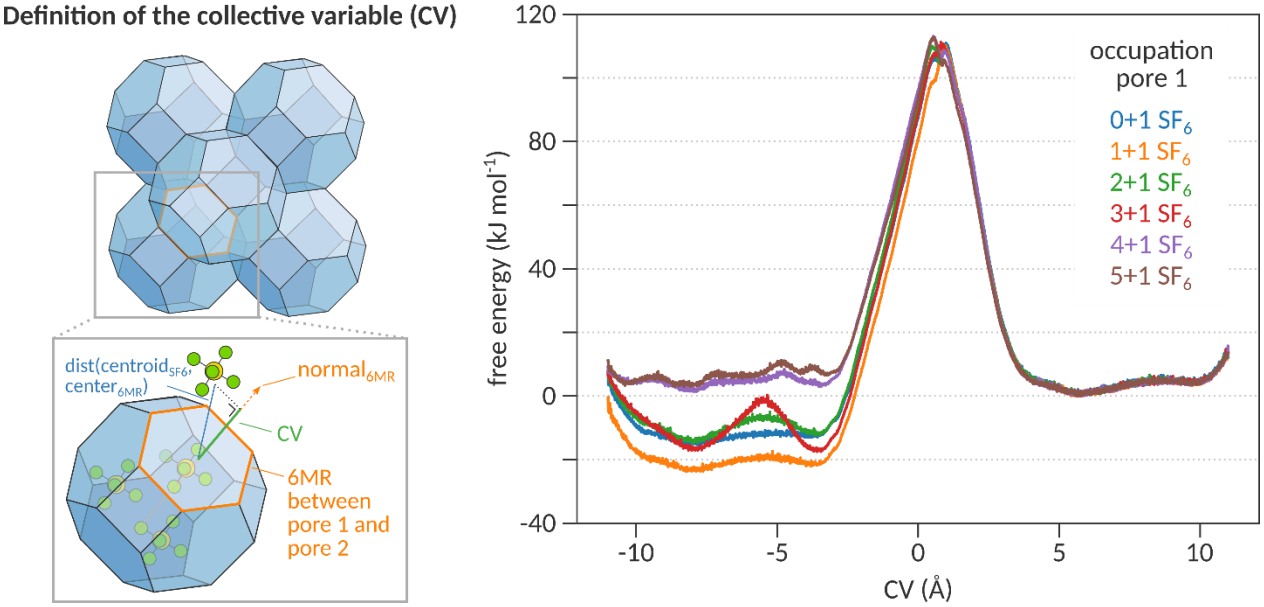

Figure S35. Left: definition of the collective variable (CV) as the projected distance of the centroid of the constrained SF_6 molecule as seen from the center of the 6MR onto the normal of the 6MR, defined in the direction from pore 1 to pore 2. Right: 300 K free energy profiles for the hopping of one SF_6 molecules from pore 1 (CV < 0 Å) to pore 2 (CV > 0 Å). In these simulations, between zero and five additional SF_6 molecules are present in pore 1, while no additional molecules are present in pore 2.

Figure S35 shows the free energy profiles that are obtained in this fashion. Given the variable loading observed for the different pores, this analysis was repeated for different loadings of the first pore. Besides the SF_6 molecule that is constrained during the simulation, between zero and five additional SF_6 molecules were present in the first pore (CV < 0 Å). In contrast, the adjacent second pore (CV > 0 Å) contains no additional molecules.

As already indicated in the main text, the forward free energy barrier in Figure S35 varies between 100 and 130 kJ mol^{-1}, depending on the number of molecules in pore 1. Moreover, it becomes the largest at intermediate loadings, as shown in Figure S34, given that the free energy of pore 1 is the lowest at that loading. This behaviour may be explained as follows. For the first transition (in blue), in which there are no other SF_6 molecules in ZIF-8 besides the one making the transition, the molecule can only interact with the

pore walls. Pore 1, which is slightly smaller than pore 2 due to the procedure with which the initial structures were generated (see section 5 above), interacts more strongly with the SF_6 molecule through dispersion and Coulomb interactions than pore 2, leading to a small asymmetry between the two pores. The forward energy barrier amounts to about 124 kJ mol^{-1} in this case. The difference between the forward and the reverse free energy barrier, 13 kJ mol^{-1}, is an indication of the extent to which small pore distortions impact the free energy barrier. When one additional SF_6 molecule is present in pore 1 (in orange), dispersive guest-guest interactions stabilise the molecules in pore 1, leading to a higher forward free energy barrier of about 132 kJ mol^{-1}. At that point, any additional SF_6 molecule leads to steric hindrance that counteracts the attractive dispersive interactions and leads to a destabilization of pore 1, as explained in the main text.
All forward and reverse free energy barriers are tabulated in Table S5.

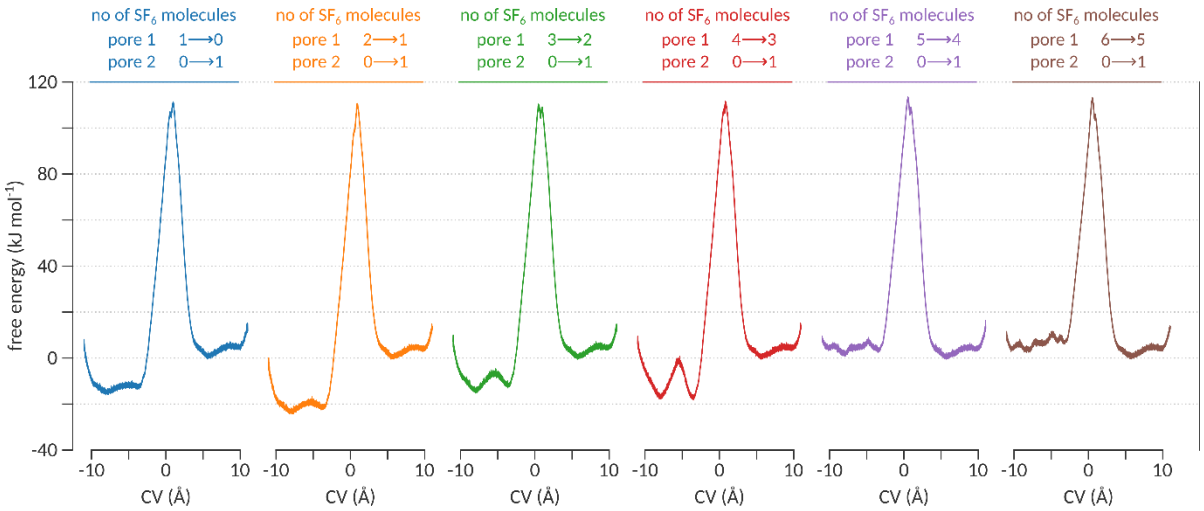

Figure S34. 300 K free energy profiles from Figure S35 as seen side-by-side.

Table S5. Forward and reverse free energy barriers at 300 K as extracted from Figure S34.

	0 extra molecules in pore 1	1 extra molecule in pore 1	2 extra molecules in pore 1	3 extra molecules in pore 1	4 extra molecules in pore 1	5 extra molecules in pore 1
forward free energy barrier (kJ mol^{-1})	124	132	122	128	110	106
reverse free energy barrier (kJ mol^{-1})	111	110	110	111	113	113

7. References

[1] K. S. Park, Z. Ni, A. P. Côté, J. Y. Choi, R. Huang, F. J. Uribe-Romo, H. K. Chae, M. O'Keeffe, O. M. Yaghi, "Exceptional chemical and thermal stability of zeolitic imidazolate frameworks", *Proc. Natl. Acad. Sci.*, 2006, **103**, 10186-10191.

[2] C. Chapados, G. Birnbaum, "Infrared absorption of SF_6 from 32 to 3000 cm^{-1} in the gaseous and liquid states", *J. Mol. Spectrosc.*, 1988, **132**, 323-351.

[3] J. Kärger, "Transport Phenomena in Nanoporous Materials", *ChemPhysChem*, 2015, **16**, 24–51.

[4] Y. Sun, S. M. J. Rogge, A. Lamaire, S. Vandenbrande, J. Wieme, C. R. Siviour, V. Van Speybroeck, J.-C. Tan, "High-rate nanofluidic energy absorption in porous zeolitic frameworks," *Nat. Mater.*, 2021, **20**, 1015-1023.

[5] L. Vanduyfhuys, S. Vandenbrande, T. Verstraelen, R. Schmid, M. Waroquier, V. Van Speybroeck, "QuickFF: A program for a quick and easy derivation of force fields for metal-organic frameworks from ab initio input," *J. Comput. Chem.*, 2015, **36**, 1015-1027.

[6] L. Vanduyfhuys, S. Vandenbrande, J. Wieme, M. Waroquier, T. Verstraelen, V. Van Speybroeck, "Extension of the QuickFF force field protocol for an improved accuracy of structural, vibrational, mechanical, and thermal properties of metal-organic frameworks," *J. Comput. Chem.,* 2018, **39**, 999-1011.

[7] A. D. Becke, "Density-functional thermochemistry. III. The role of exact exchange," *J. Chem. Phys.*, 1993, **98**, 5648.

[8] P. J. Stephens, F. J. Devlin, C. F. Chabalowski, M. J. Frisch, "Ab initio calculation of vibrational absorption and circular dichroism using density functional force fields," *J. Phys. Chem.*, 1994, **98**, 11623-11627.

[9] M. J. Frisch, G. W. Trucks, H. B. Schlegel, G. E. Scuseria, M. A. Robb, J. R. Cheeseman, G. Scalmani, V. Barone, G. A. Petersson, H. Nakatsuji, X. Li, M. Caricato, A. V. Marenich, J. Bloino, B. G. Janesko, R. Gomperts, B. Mennucci, H. P. Hratchian, J. V. Ortiz, A. F. Izmaylov, J. L. Sonnenberg, D. Williams-Young, F. Ding, F. Lipparini, F. Egidi, J. Goings, B. Peng, A. Petrone, T. Henderson, D. Ranasinghe, V. G. Zakrzewski, J. Gao, N. Rega, G. Zheng, W. Liang, M. Hada, M. Ehara, K. Toyota, R. Fukuda, J. Hasegawa, M. Ishida, T. Nakajima, Y. Honda, O. Kitao, H. Nakai, T. Vreven, K. Throssell, J. A. Montgomery Jr., J. E. Peralta, F. Ogliaro, M. J. Bearpark, J. J. Heyd, E. N. Brothers, K. N. Kudin, V. N. Staroverov, T. A. Keith, R. Kobayashi, J. Normand, K. Raghavahari, A. P. Rendell, J. C. Burant, S. S. Iyengar, J. Tomasi, M. Cossi, J. M. Milliam, M. Klene, C. Adamo, R. Cammi, J. W. Ochterski, R. L. Martin, K. Morokuma, O. Farkas, J. B. Foresman, D. J. Fox, "Gaussian 16, Revision A.03," *Gaussian, Inc., Wallingford CT,* 2016.

[10] T. Verstraelen, S. Vandenbrande, F. Heidar-Zadeh, L. Vanduyfhuys, V. Van Speybroeck, M. Waroquier, P. W. Ayers, "Minimal Basis Iterative Stockholder: Atoms in molecules for force-field development," *J. Chem. Theory Comput.*, 2016, **12**, 3894-3912.

[11] J. Chen, T. J. Martínez, "QTPIE: Charge transfer with polarization current equalization. A fluctuating Charge model with correct asymptotics," *Chem. Phys. Lett.*, 2007, **438**, 315-320.

[12] N. L. Allinger, Y. H. Yuh, J. H. Lii, "Molecular mechanics. The MM3 force field for hydrocarbons. 1," *J. Am. Chem. Soc.*, 1989, **111**, 8551-8566.

[13] P. Cnudde, R. Demuynck, S. Vandenbrande, M. Waroquier, G. Sastre, V. Van Speybroeck, "Light olefin diffusion during the MTO process on H-SAPO-34: A complex interplay of molecular factors," *J. Am. Chem. Soc.*, 2020, **142**, 6007-6017.

[14] S. M. J. Rogge, L. Vanduyfhuys, A. Ghysels, M. Waroquier, T. Verstraelen, G. Maurin, V. Van Speybroeck, "A comparison of barostats for the mechanical characterization of metal-organic frameworks," *J. Chem. Theory Comput.*, 2015, **11**, 5583-5597.

[15] T. Verstraelen, L. Vanduyfhuys, S. Vandenbrande, S. M. J. Rogge, "Yaff, Yet Another Force Field," Available online at http://molmod.ugent.be/software.

[16] S. Plimpton, "Fast parallel algorithms for short-range molecular dynamics," *J. Comput. Phys.*, 1995, **117**, 1-19.

[17] S. Nosé, "A molecular dynamics method for simulations in the canonical ensemble," *Mol. Phys.*, 1984, **52**, 255-268.

[18] S. Nosé, "A unified formulation of the constant temperature molecular dynamics methods," *J. Chem. Phys.*, 1984, **81**, 511-519.

[19] W. G. Hoover, "Canonical dynamics: Equilibrium phase-space distributions," *Phys. Rev. A*, 1985, **31**, 1695-1697.

[20] G. J. Martyna, M. L. Klein, M. E. Tuckerman, "Nosé-Hoover chains: The canonical ensemble via continuous dynamics," *J. Chem. Phys.*, 1992, **97**, 2635-2643.

[21] G. J. Martyna, D. J. Tobias, M. L. Klein, "Constant pressure molecular dynamics algorithms," *J. Chem. Phys.*, 1994, **101**, 4177-4189.

[22] G. J. Martyna, M. E. Tuckerman, D. J. Tobias, M. L. Klein, "Explicit reversible integrators for extended systems dynamics," *Mol. Phys.*, 1996, **87**, 1117-1157.

[23] P. P. Ewald, "Die Berechnung Optischer und Elektrostatischer Gitterpotentiale," *Ann. Phys.*, 1921, **369**, 253-287.

[24] S. Kumar, J. M. Rosenberg, D. Bouzida, R. H. Swendsen, P. A. Kollman, "The weighted histogram analysis method for free-energy calculations on biomolecules. I. The method," *J. Comput. Chem.*, 1992, **13**, 1011-1021.

[25] M. Souaille, B. Roux, "Extension to the weighted histogram analysis method: Combining umbrella sampling with free energy calculations," *Comput. Phys. Commun.*, 2001, **135**, 40-57.